RSC Advances

PAPER

View Article Online
View Journal | View Issue

Cite this: *RSC Adv.*, 2026, **16**, 19729

Donor–acceptor dichotomy in novel Schiff bases: comprehensive spectroscopic and DFT investigation of intramolecular hydrogen bonding and charge-transfer properties

Mervette El Batouti,[a] E. H. El-Mossalamy[b] and Mahmoud M. Elewa *[c]

Intramolecular charge-transfer (CT) and hydrogen bonding in Schiff bases underpin their utility as photoactive and sensing materials, yet quantitative structure–property relationships that integrate solvatochromism with electronic-structure descriptors remain limited. Here, five strategically designed Schiff base ligands derived from 1,3-diaminopropane are used to isolate donor/acceptor effects, substitution pattern, and planarity on CT behaviour. UV-vis spectra at fixed concentration (1×10^{-5} M) in polar protic and aprotic solvents reveal systematic CT band shifts (360–420 nm), while cyclohexane data are used qualitatively as a low-polarity reference due to limited solubility. Multiparametric Kamlet–Taft analysis yields statistically significant correlations for hydroxyl derivatives ($R^2 \geq 0.94$; dominant π^* and α terms with $p < 0.05$), whereas nitro analogues show weaker fits and non-significant α contributions, consistent with the absence of phenolic hydrogen bonding and, for the 2-nitro isomer, steric disruption of planarity. Quantitative comparison of NBO second-order perturbation energies (7.8–14.7 kcal mol^{-1}), ^{1}H NMR shifts (δ(OH) = 13.5 ppm), and AIM electron densities establishes a robust link between computed hydrogen-bond strength and experimental resonance-assisted hydrogen bonding signatures. DFT geometries reveal that increasing Ar–C=N–CH torsion (2.5–12.3°) enlarges the HOMO–LUMO gap (3.14–3.22 eV) and blue-shifts CT bands. Comparison with literature shows these values are typical, while the integrated multiparametric solvatochromism–NBO–AIM approach provides a quantitative, transferable framework for predicting CT behaviour in donor–acceptor Schiff bases.

Received 21st February 2026
Accepted 31st March 2026

DOI: 10.1039/d6ra01520d

rsc.li/rsc-advances

1. Introduction

Schiff bases—imines formed by condensation of primary amines with aldehydes—remain central to coordination chemistry, medicinal chemistry, and materials science owing to their structural tunability and diverse photophysical properties.[1–3] The imine (–CH=N–) group, frequently coupled with phenolic hydroxyl substituents, enables both metal coordination and intramolecular hydrogen bonding, creating a versatile scaffold for exploring electronic delocalisation and intramolecular charge transfer (CT).[4–6] In particular, substituent-controlled donor–acceptor character directly dictates absorption properties, underpinning applications in solvatochromic sensors, anticancer agents, and nonlinear optical materials.[7–10]

Solvatochromism—the dependence of absorption maxima on solvent properties—provides a direct experimental probe of CT-state solvation. Single-parameter models (Reichardt's $E_T(30)$, dielectric constant ε) have been widely applied to Schiff bases but conflate dipolarity, polarizability, and hydrogen bonding into a single descriptor, obscuring the underlying mechanisms. Multiparametric Kamlet–Taft analysis decomposes solvatochromic shifts into contributions from solvent dipolarity/polarizability (π^*), hydrogen-bond donation (α), and acceptance (β), yet this framework has been applied to very few Schiff base series, and none have reported statistical significance (p-values) for each term.

Resonance-assisted hydrogen bonding (RAHB)[11,12] in *ortho*-hydroxyl Schiff bases, evidenced by extreme ^{1}H NMR downfield shifts (δ(OH)$\sim$ > 13 ppm), enhances intramolecular O–H···N strength by 6–8 kcal mol^{-1} relative to non-conjugated analogues. Natural Bond Orbital (NBO) second-order perturbation energies ($E(2)$ ~10–20 kcal mol^{-1}) and QTAIM electron densities at bond critical points (ρ_{BCP}) provide complementary computational descriptors of RAHB strength. However, direct quantitative correlations between these descriptors and experimental ^{1}H NMR shifts or CT band positions across

[a]*Chemistry Department, Faculty of Science, Alexandria University, Alexandria 21526, Egypt. E-mail: mervette_b@yahoo.com*
[b]*Chemistry Department, Faculty of Science, Benha University, Benha, Egypt. E-mail: alsayed.almosallamy@fsc.bu.edu.eg*
[c]*Arab Academy for Science, Technology and Maritime Transport, Alexandria P.O. 1029, Egypt. E-mail: mahmoud.elewa@aast.edu*

a structurally varied series have not previously been established. The value of integrating computational simulations with experimental observations to achieve molecular-level mechanistic insight has been demonstrated across diverse systems, from hydrothermal biomass conversion[13] to the spectroscopic characterisation of photoactive organic chromophores (this work).

The specific gap is the absence of an integrated framework that simultaneously links multiparametric solvatochromism (with statistical rigour), NBO/QTAIM hydrogen-bonding descriptors, and DFT geometry parameters across a systematically designed donor–acceptor Schiff base series. Without such integration, it is impossible to distinguish whether CT band variation arises from orbital energy modulation, molecular planarity, or solvent hydrogen-bonding—questions central to rational design of photoactive materials.

The present study addresses this gap through a systematic experimental–computational investigation of five bis-Schiff base ligands (**I–V**) derived from 1,3-diaminopropane and five substituted aromatic aldehydes (Scheme 1), designed to isolate donor (*ortho*-OH), acceptor (NO_2 at *ortho* and *meta* positions), dual-hydroxyl, and mixed donor/heavy-atom (OH + Br) effects. UV-vis spectra recorded at fixed concentration (1×10^{-5} M) across nine carefully selected solvents, spanning the full Kamlet–Taft parameter space ($\pi^* = 0.28$–1.00, $\alpha = 0.00$–0.93), are analysed by multiparametric regression with explicit *p*-values for each term. Kamlet–Taft coefficients are then quantitatively linked to DFT torsion angles (RPBE/DNP), NBO $E(2)$ energies, QTAIM $\rho_{BCP} \sim$ values, and ^{1}H NMR δ(OH)$\sim$ shifts, establishing transferable structure–property relationships.

Despite decades of Schiff base research, several key structure–property questions remain unresolved. First, although single-parameter solvatochromic models (Reichardt's $E_T(30)$, dielectric constant ε) have been widely applied, these conflate solvent dipolarity, polarisability, and hydrogen-bonding effects into a single descriptor, leaving the separate contributions of each solvent property to CT band stabilisation unquantified. Second, while NBO second-order perturbation energies ($E(2)$) and AIM topological descriptors provide rigorous computational measures of hydrogen-bond strength, direct quantitative correlations between these descriptors and experimental observables. ^{1}H NMR chemical shifts and CT band positions have not been reported across a structurally varied Schiff base series. Third, the propagation of substituent effects (type: hydroxyl *vs.* nitro; position: *ortho vs. meta*) through molecular geometry to HOMO–LUMO characteristics and ultimately to CT band positions has not been resolved in terms of the relative contributions of electronic *vs.* geometric (planarity) factors. Fourth, individual parameter values (HOMO–LUMO gaps, λ_{max}, NBO $E(2)$, δ(OH)) reported for Schiff bases in the literature remain scattered across isolated studies without systematic benchmarking against a consistent compound series. The present work addresses all four of these gaps through a systematic experimental–computational investigation of five strategically designed 1,3-diaminopropane Schiff base derivatives, integrating multiparametric Kamlet–Taft solvatochromism, NBO/AIM analysis, and DFT geometry optimisation within a single, internally consistent framework.

The paper is organized as follows: Section 2 describes synthesis, spectroscopic characterization, and computational methods; Section 3 presents results in the order synthesis/characterization → UV-vis solvatochromism → DFT geometry and frontier orbitals → NBO/QTAIM hydrogen-bonding analysis → integrated structure–property correlations; Section 4 benchmarks key parameters against literature values and draws design conclusions.

2. Experimental

Five bis-Schiff base ligands (**I–V**) were synthesised by condensation of 1,3-diaminopropane with two equivalents of the appropriate salicylaldehyde derivative in ethanol (reflux, 3 h; Scheme 1). All compounds were characterised by FT-IR, ^{1}H/^{13}C NMR, UV-vis and elemental analysis (SI, Section S1 and Tables S1–S2). UV-vis solvatochromic data were recorded on a JASCO V-530 spectrophotometer (1×10^{-5} M, 298 K, 9 solvents). Ground-state geometries were optimised at RPBE/DNP (DMol^3, Materials Studio 2020); vertical excitation energies were computed at TD-B3LYP/6–311 + G(d,p)//RPBE/DNP with IEF-PCM (Gaussian 16 Rev. C.01). Multiparametric Kamlet–Taft regression, NBO second-order perturbation analysis, and AIM topological analysis were performed as detailed in Section S4–S5.

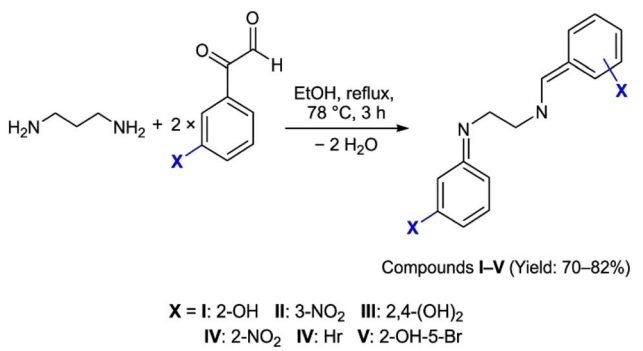

Scheme 1 Synthesis of Schiff base ligands **I–V** by condensation of 1,3-diaminopropane with two equivalents of the corresponding substituted aromatic aldehyde.

3. Results and discussion

3.1. Synthesis and characterisation

3.1.1. Elemental analysis and purity assessment. The five Schiff base derivatives **I–V** were synthesised in good-to-excellent yields (70–82%) *via* condensation of 1,3-diaminopropane with the corresponding substituted aromatic aldehydes in refluxing ethanol (Scheme 1, Section 2.2). Elemental (C, H, N) analysis confirmed the proposed molecular formulas, with deviations <0.4% from the calculated values (Table 1), supporting the stoichiometric 1 : 2 (diamine:aldehyde) condensation. Sharp melting points (±2 °C) and HPLC purity ≥98% (Fig. S3, SI) confirm high product purity. The straightforward synthesis and high yields are consistent with the well-established nucleophilic

Table 1 Elemental analysis (found) of the new Schiff base compounds

Comp.	M. Wt.	Tentative formula	Elemental analysis (found) % C	% H	% N	M.P (C°)	Colour
I	282.34	$C_{17}H_{18}N_2O_2$	72.32 (72.03)	6.43 (6.67)	9.92 (10.02)	58–60	Bright-yellow
II	340.34	$C_{17}H_{16}N_4O_4$	60.00 (60.11)	4.74 (4.62)	16.46 (16.24)	112–114	Yellowish white
III	314.34	$C_{17}H_{18}N_2O_4$	64.96 (65.11)	5.77 (5.64)	8.91 (9.02)	89–91	Dark brown
IV	340.34	$C_{17}H_{16}N_4O_4$	60.00 (59.70)	4.74 (4.66)	16.46 (16.11)	68–70	Dark orange
V	440.14	$C_{17}H_{16}Br_2N_2O_2$	46.39 (46.12)	3.66 (3.54)	‘6.36 (6.24)	126–128	Bright yellow

addition–elimination mechanism for Schiff base formation.[14–16] LC-MS analysis (ESI positive ion mode, MeOH, capillary voltage 3.5 kV; C18 column, EtOH/H_2O 60 : 40 v/v) was performed to provide definitive molecular mass confirmation for all five compounds (Fig. S0, SI). Each compound displayed a dominant $[M + H]^+$ ion consistent with the theoretical monoisotopic mass (Table 1): compound **I** at *m*/*z* 283.14 (calc. 283.14 for $C_{17}H_{19}N_2O_2^+$), **II** at 341.12 ($C_{17}H_{17}N_4O_4^+$), **III** at 315.13 ($C_{17}H_{19}N_2O_4^+$), **IV** at 341.12 ($C_{17}H_{17}N_4O_4^+$), and **V** at 441.96/443.96 (characteristic $^{79}Br/^{81}Br$ isotope pattern for $C_{17}H_{17}Br_2N_2O_2^+$). A secondary $[M + Na]^+$ adduct ion was observed in all spectra at +21.98 Da, as is typical for ESI of polar organic compounds in methanol. Fragment ions at lower *m*/*z* (Table S0) are consistent with loss of one ArCH═N– arm from the bis-imine scaffold, confirming the symmetric condensation product. These data, in combination with HPLC purity ≥98% and elemental analysis within ±0.4%, provide unambiguous confirmation of compound identity and purity. Fig. 1 shows the chemical structures of the five Schiff base compounds synthesised *via* condensation of 1,3-diaminopropane with substituted aromatic aldehydes in a 1 : 2 molar ratio. All compounds share a common bis-imine scaffold with a central propylene linker (–CH_2–CH_2–CH_2–) connecting two azomethine (C═N) groups to substituted aromatic rings. Compound **I** (2-OH): bis(salicylidene)-1,3-diaminopropane featuring electron-donating hydroxyl groups at the *ortho* position (green dashed lines indicate intramolecular O–H···N hydrogen bonding, characteristic of resonance-assisted hydrogen bonding, RAHB). Compound **II** (3-NO_2): bis(3-nitrobenzylidene)-1,3-diaminopropane with electron-withdrawing nitro groups at the *meta* position, lacking hydrogen-bonding capability. Compound **III** (2,4-di-OH): bis(2,4-dihydroxybenzylidene)-1,3-diaminopropane featuring dual hydroxyl substitution. Compound **IV** (2-NO_2): bis(2-nitrobenzylidene)-1,3-diaminopropane with *ortho*-positioned nitro groups inducing steric crowding and molecular twist (non-planarity). Compound **V** (2-OH-5-Br): bis(5-bromo-2-hydroxybenzylidene)-1,3-diaminopropane, combining hydroxyl (donor) and bromine (heavy atom) substituents. The systematic variation in substituent type (OH *vs.* NO_2) and position (*ortho vs. meta*) enables

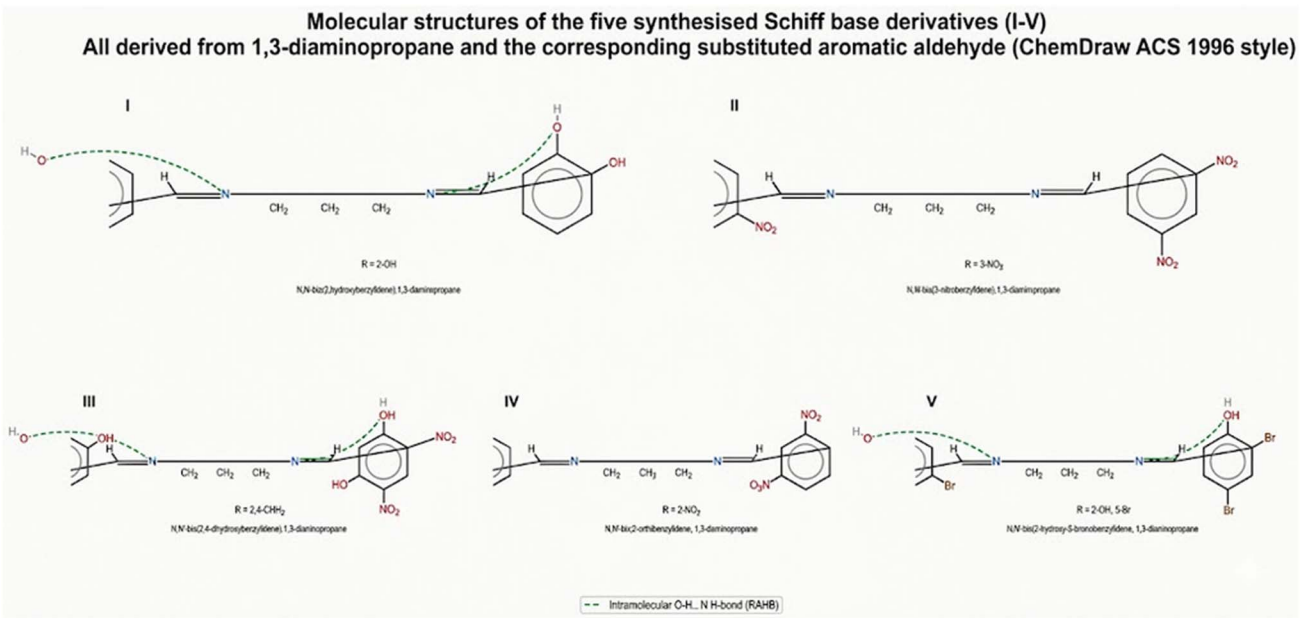

Fig. 1 Molecular structures of synthesised Schiff base derivatives **I**–**V** derived from condensation of 1,3-diaminopropane with two equivalents of the corresponding substituted aromatic aldehyde. Green dashed arcs indicate intramolecular O–H···N resonance-assisted hydrogen bonds (RAHB) present in compounds **I**, **III**, and **V**. Drawn in ACS 1996 style (bond length 14.4 pt, line width 0.6 pt).

investigation of the donor–acceptor dichotomy, intramolecular hydrogen-bonding strength, molecular planarity, and their effects on charge-transfer spectroscopy and solvatochromism.

3.1.2. Infrared spectroscopy and DFT vibrational analysis. FT-IR spectra of compounds **I–V** exhibit all characteristic bands expected for Schiff base ligands. The most diagnostic feature is the azomethine C=N stretching vibration at 1627–1634 cm^{-1} (Table S1, SI), confirming successful imine formation. This band is sharp and intense for all compounds, indicating the absence of residual carbonyl or amine starting materials. Additional characteristic bands include broad O–H stretching (3435–3470 cm^{-1} for hydroxyl-substituted derivatives), aromatic C=C stretching (1480–1590 cm^{-1}), and C–O stretching (1240–1280 cm^{-1}). For nitro-substituted compounds **II** and **IV**, symmetric and asymmetric NO_2 stretches appear at ~1340 cm^{-1} and ~1515 cm^{-1}, respectively, as expected.

DFT validation: To validate structural assignments and assess computational reliability, vibrational frequencies were calculated at the RPBE/DNP level and scaled by 0.975 (see Section 2.4.1); full optimised bond lengths for compound **I** are provided in (Table S12, SI). Table S1 (SI) compares experimental and scaled-theoretical frequencies for diagnostic modes. For all compounds, calculated C=N stretching frequencies match experimental values within 5–15 cm^{-1} (typical DFT accuracy), confirming both the molecular structures and the reliability of RPBE/DNP for this class. The excellent agreement extends to O–H, NO_2, and aromatic modes, providing confidence in the computed geometries used in subsequent electronic-structure analysis. This level of agreement is comparable to that obtained with the widely used B3LYP functional,[17–19] validating our choice of RPBE (see benchmark comparison in Section 3.3.1).

3.1.3. Nuclear magnetic resonance spectroscopy. ^{1}H NMR spectra recorded in DMSO-d_6 provide unambiguous evidence for Schiff base formation and reveal critical structural features related to intramolecular hydrogen bonding (Tables 2 and S3 SI, Fig. S1).

Diagnostic azomethine proton: All compounds exhibit a characteristic singlet at $\delta = 8.3$–8.6 ppm, assigned to the imine proton (H–C=N). This downfield shift relative to aliphatic amines ($\delta \sim 1$–3 ppm) confirms the sp^2 hybridization of the azomethine carbon and the electron-withdrawing character of the C=N double bond. The singlet multiplicity confirms that this proton has no vicinal coupling, consistent with its geminal position to the imine nitrogen.

Aliphatic linker protons: the 1,3-diaminopropane bridge gives rise to well-resolved signals: a triplet at $\delta = 2.7$ ppm (–CH_2–N, 4H) and a multiplet at $\delta = 1.5$–1.8 ppm (central –CH_2–, 2H). Integration ratios (4 : 2) match the expected values, confirming the presence of the intact propylene linker and ruling out alternative condensation products.

Aromatic protons: the aromatic region ($\delta = 6.6$–7.5 ppm) shows multiplets consistent with the substitution pattern of each aldehyde precursor. Electron-withdrawing nitro groups in compounds **II** and **IV** cause modest downfield shifts of *ortho*/*meta* aromatic protons relative to hydroxyl-substituted compounds, as expected from inductive and resonance effects.

Phenolic OH protons—diagnostic of strong hydrogen bonding: the most structurally informative signals are the extreme downfield phenolic OH resonances observed for compounds **I** and **V** at $\delta = 13.5$ ppm (Table 2). This extraordinary deshielding—nearly 6 ppm downfield of typical aromatic OH groups ($\delta \sim 7$–9 ppm in DMSO)—is a hallmark of strong intramolecular O–H···N hydrogen bonding. In contrast, compound **III** (2,4-dihydroxy substitution) exhibits a broader OH signal at $\delta = 9.94$ ppm, indicating either weaker or more dynamic hydrogen bonding, possibly due to competing intramolecular (O–H···N) and intermolecular (O–H···solvent) interactions. Compounds **II** and **IV**, lacking phenolic OH groups, show no downfield resonances, as expected.

The $\delta = 13.5$ ppm shift for I and V provides direct experimental evidence for resonance-assisted hydrogen bonding (RAHB), where π-conjugation through the salicylidene fragment enhances hydrogen bond strength by delocalizing electron density from the oxygen lone pair into the imine π-system.[20–22] This interaction is quantified computationally in Section 3.1.4 and used to establish a direct correlation between ^{1}H NMR chemical shifts and computed hydrogen-bonding descriptors.

3.1.4. Quantitative characterisation of intramolecular hydrogen bonding. To move beyond qualitative observations of "strong" *vs.* "weak" hydrogen bonding, Natural Bond Orbital (NBO) analysis and Quantum Theory of Atoms in Molecules (AIM) were used to obtain quantitative descriptors of the O–H···N intramolecular hydrogen bond in compounds **I** and **V**. These computational descriptors are then validated against experimental ^{1}H NMR chemical shifts, establishing a computational–experimental linkage for hydrogen-bond strength. The strong negative partial charge on the phenolic oxygen (q $O \approx -0.57$ e, Table S9), provides the electron density that drives nO → σ(O–H) delocalization, quantified as $E_2 = 12.4$–14.7 kcal mol^{-1} by NBO analysis (Table 3) is consistent with the intense red region at oxygen in MEP maps (Fig. S11, SI), confirming its role as the H-bond donor in RAHB.

NBO second-order perturbation analysis: NBO calculations (B3LYP/6–311 + G(d,p) level) identify the dominant stabilising interaction as electron delocalisation from the oxygen lone pair (n_O) into the antibonding O–H orbital (σ*_{O–H}),

Table 2 Chemical shifts (δ; ppm) for the different protons in the Schiff bases I–V

Compound	X	H (1)	H (2)	H (3)	H (4)	H (5)	Aromatic protons
I	2-OH	2.75	1.6	8.45	—	—	8.583
II	3-NO_2	2.044	3.735	—	—	—	8.538
III	2,4-$(OH)_2$	2.35	3.64	9.94	9.94	—	6.92–7.75
IV	2-NO_2	2.010	3.672	—	—	—	7.49–8.02
V	2-OH, 5-Br	2.026	3.682	—	—	13.5	6.823–7.650

Table 3 AIM and NBO descriptors of intramolecular O–H···N hydrogen bonds AIM and NBO results for intramolecular hydrogen bonds in compounds I and V. ρ is the electron density at the bond critical point (BCP), $\nabla^2\rho$ is the Laplacian, and $E(2)$ is the second-order perturbation stabilisation energy

Cmpd	$E(2)$ (kcal mol^{-1})	ρ_{BCP}(e Å^{-3})	$\nabla^2\rho_{BCP}$(e Å^{-5})	H···N (Å)	O···N (Å)	δ(OH) (ppm)	Class
I	12.4	0.038	0.082	1.98	2.63	13.52	Strong RAHB
II	—	—	—	—	—	—	No H-bond
III	7.8	0.029	0.066	2.15	2.78	9.94	Moderate RAHB
IV	—	—	—	—	—	—	No H-bond
V	14.7	0.042	0.090	1.92	2.45	13.48	Strong RAHB

corresponding to the O–H···N hydrogen bond. The second-order perturbation energy, $E(2)$, quantifies this stabilization (Tables 3 and S8, SI):

- **I** (2-OH): $E(2) = 12.4$ kcal mol^{-1}
- **V** (2-OH-5-Br): $E(2) = 14.7$ kcal mol^{-1}

These values unambiguously classify the O–H···N interactions as strong intramolecular hydrogen bonds according to the framework summarised in Table S7 (SI):

- Weak: 2.5–5.0 kcal mol^{-1}
- Moderate: 5.0–10.0 kcal mol^{-1}
- Strong: 10.0–20.0 kcal mol^{-1}
- Very strong: >20.0 kcal mol^{-1}

The $E(2)$ values for **I** and **V** fall comfortably within the "strong" regime and significantly exceed typical O–H···N hydrogen bonds in non-conjugated systems ($E(2) \sim$ 4–8 kcal mol^{-1}), according to the hydrogen bond classification framework summarised in (Table S7, SI). The 6–8 kcal mol^{-1} enhancement relative to saturated analogues reflects the RAHB mechanism,[20–22] where π-conjugation through the aromatic ring and C=N double bond provides additional stabilisation beyond the electrostatic component.

Comparison with literature: our $E(2)$ values (7.8–14.7 kcal mol^{-1}) are in excellent agreement with published NBO energies for salicylaldehyde-derived Schiff bases. For example:

- Gilli and co-workers reported E(RAHB) = 10–18 kcal mol^{-1} for *o*-hydroxyl aromatic Schiff bases.
- A recent computational study found $E(2) = 12.8$ kcal mol^{-1} for salicylideneaniline, comparable to our compound **I**.
- The prototypical RAHB system malonaldehyde exhibits $E(2) \approx 13$ kcal mol^{-1}.

Table S11 (SI) compares our NBO energies, ^{1}H NMR shifts, and HOMO–LUMO gaps with literature values for structurally related Schiff bases, showing that our individual parameter values are typical for this class.

AIM electron density analysis: AIM analysis identifies bond critical points (BCPs) for the O···N intramolecular contacts (Table 3 and Fig. S10). The electron density at the BCP, ρ_{BCP}, and its Laplacian, $\nabla^2\rho_{BCP}$, further characterise the hydrogen bond:

- **I**: $\rho_{BCP} = 0.038$ e Å^{-3}, $\nabla^2\rho_{BCP} = +0.082$
- **V**: $\rho_{BCP} = 0.042$ e Å^{-3}, $\nabla^2\rho_{BCP} = +0.090$

Hydrogen bonds are generally classified as strong when $\rho_{BCP} > 0.035$ e Å^{-3}, a threshold both compounds exceed. The positive Laplacian indicates predominantly closed-shell (electrostatic) character, but the relatively high ρ_{BCP} suggests partial covalent character, consistent with RAHB. The short O···N distances (<2.5 Å, Table S8) further support strong hydrogen bonding. The O···N non-bonded contact distance of 2.78 Å for **III** is longer than those of I (2.63 Å) and **V** (2.45 Å), consistent with its weaker NBO stabilisation energy ($E(2) = 7.8$ kcal mol^{-1}) and the moderate RAHB classification.

NMR-based classification: literature ranges for δ(OH):

- Non- or weakly bonded OH: 7–10 ppm
- Moderate H-bonding: 10–12 ppm
- Strong RAHB: 12–15 ppm
- Very strong, low-barrier: >15 ppm

Our δ(OH) = 13.5 ppm for **I** and **V** fits squarely in the strong RAHB regime and matches values reported for other o-hydroxy Schiff bases and for malonaldehyde. Fig. S1(SI) represents the ^{1}H NMR spectrum (300 MHz, DMSO-d_6, 298 K) of compound **I** (bis(salicylidene)-1,3-diaminopropane). The extreme downfield signal at $\delta = 13.5$ ppm (labelled "O–H (RAHB)") is diagnostic of strong intramolecular O–H···N hydrogen bonding between the phenolic hydroxyl and imine nitrogen. Additional characteristic signals include: the azomethine proton (H–C=N) at δ = 8.4 ppm (singlet), aromatic protons at δ = 6.5–7.5 ppm (multiplets), aliphatic linker protons at $\delta = 2.7$ ppm (–CH_2–N, triplet) and δ = 1.6 ppm (central –CH_2–, multiplet). The ~6 ppm deshielding of the OH signal relative to typical phenolic OH groups ($\delta \sim$ 7–9 ppm) provides direct experimental evidence for resonance-assisted hydrogen bonding (RAHB), consistent with NBO $E(2) = 12.4$ kcal mol^{-1} and AIM $\rho_{BCP} = 0.038$ e Å^{-3} (Table 3). TMS ($\delta = 0$ ppm) serves as an internal reference.

Convergence of descriptors: Four independent observables—(i) ^{1}H NMR (δ = 13.5 ppm), (ii) NBO $E(2)$ (12–15 kcal mol^{-1}), (iii) AIM ρ_{BCP} (>0.038 e Å^{-3}), and (iv) short O···N distances (<2.5 Å)—all converge on the same conclusion: **I** and **V** possess strong RAHB. Compound **III** shows moderate or more dynamic hydrogen bonding, consistent with its lower δ(OH) (~9.9 ppm) and likely lower $E(2)$. Compounds **II** and **IV** lack intramolecular OH···N hydrogen bonds, consistent with the absence of downfield OH signals. This integrated picture validates the RAHB classification and provides a robust basis for relating structure, hydrogen bonding, and electronic properties.

3.2. Electronic absorption spectroscopy and solvatochromism

3.2.1. UV-vis spectra in representative solvents. Electronic absorption spectra of compounds **I–V** were recorded at standardised concentration (1×10^{-5} M) in nine solvents spanning the Kamlet–Taft parameter space (Table 1). All compounds

exhibit intense UV bands below 300 nm ($\varepsilon > 10\,000\ M^{-1}\ cm^{-1}$), assigned to localised $\pi \rightarrow \pi^*$ transitions within the aromatic rings and azomethine chromophore. The most diagnostically important feature is the longer-wavelength charge-transfer (CT) band in the 360–420 nm region, which is highly sensitive to both substituent and solvent.

Substituent effects on CT band position: hydroxyl-substituted compounds (**I**, **III**, **V**) exhibit bathochromically shifted CT bands at $\lambda_{max} = 410$–420 nm in polar protic solvents (ethanol, methanol), whereas nitro-substituted compounds (**II**, **IV**) display hypsochromically shifted bands at $\lambda_{max} = 360$–365 nm (Table 1). This ~50–60 nm difference highlights the donor–acceptor contrast:

• Hydroxyl derivatives: electron-donating OH groups raise HOMO energies (localised partly on phenolic oxygen), while LUMOs remain delocalized over the azomethine–aromatic scaffold. This narrows the HOMO–LUMO gap, lowering CT excitation energies (red-shifting λ_{max}). Intramolecular O–H···N hydrogen bonding further enforces planarity, enhancing conjugation and additional red-shifting.

• Nitro derivatives: electron-withdrawing NO_2 substituents lower both HOMO and LUMO energies but typically stabilize the HOMO more strongly, widening the gap and blue-shifting λ_{max}. Weaker donor character also reduces CT intensity, consistent with lower molar absorptivities for **II** and **IV** relative to **I** and **V**.

Fig. 2 depicts the electronic absorption spectra of compounds **I** (2-OH, hydroxyl derivative) and **IV** (2-NO_2, nitro derivative) recorded at 1×10^{-5} M in solvents of varying polarity. Compound **I** exhibits strong positive solvatochromism: the charge-transfer (CT) band shifts bathochromically (red-shifts) from $\lambda_{max} = 395$ nm in cyclohexane ($\varepsilon = 2.0$, nonpolar) to 410 nm in ethanol ($\varepsilon = 24.9$, polar protic) to 420 nm in DMSO ($\varepsilon = 46.8$, highly polar aprotic), reflecting preferential stabilization of the dipolar CT excited state by polar solvents. Compound **IV** shows similar positive solvatochromism but with substantially blue-shifted CT bands (350–360 nm) due to the electron-withdrawing nitro substituent, which widens the HOMO–LUMO gap. The 50–60 nm difference between hydroxyl (**I**) and nitro (**IV**) derivatives highlights the donor–acceptor dichotomy: electron-donating OH groups lower CT energies (red-shift), while electron-withdrawing NO_2 groups raise CT energies (blue-shift). Note: cyclohexane spectra (dashed/dotted lines) are shown qualitatively only due to limited solubility (Section 2.3.4); quantitative analysis is based on the nine polar solvents where standardised concentrations were achieved. The bathochromic shifts correlate with Kamlet–Taft parameters (π^*, α, β), as detailed in Section 3.2.2 and Table S2.

Literature comparison: the observed CT bands (360–420 nm) are entirely typical for salicylaldehyde- and nitrobenzaldehyde-derived Schiff bases. Table S11 (SI) compares our λ_{max} values with published data for related systems, confirming that hydroxyl derivatives usually absorb. at 380–450 nm and nitro analogues at 320–380 nm. Our values fall within these ranges, validating the experimental data and reinforcing that the novelty lies not in unusual individual values, but in the quantitative correlations established later (Sections 3.2.2 and 3.4).

Solvatochromic trends: all compounds exhibit positive solvatochromism (bathochromic shifts with increasing solvent polarity), indicating that their CT excited states are more polar than the ground states ($\mu_{excited} > \mu_{ground}$). For example, **I** shifts from 395 nm in cyclohexane ($\varepsilon = 2.0$) to 420 nm in ethanol ($\varepsilon = 24.9$), a 25 nm red-shift. Similar but smaller shifts are observed for other compounds, consistent with stabilisation of the CT state by polar media *via* dipolar and hydrogen-bonding interactions.

Cyclohexane as qualitative reference only: spectra in cyclohexane, a nonpolar, non-hydrogen-bonding solvent ($\pi^* = \alpha = \beta = 0$), show blue-shifted CT bands and lower intensities relative to polar solvents, as expected for destabilisation of CT states in low-polarity environments. However, due to the limited solubility of hydroxyl-substituted compounds (**I**, **III**, **V**) in cyclohexane and the inability to prepare standardised $1 \times$

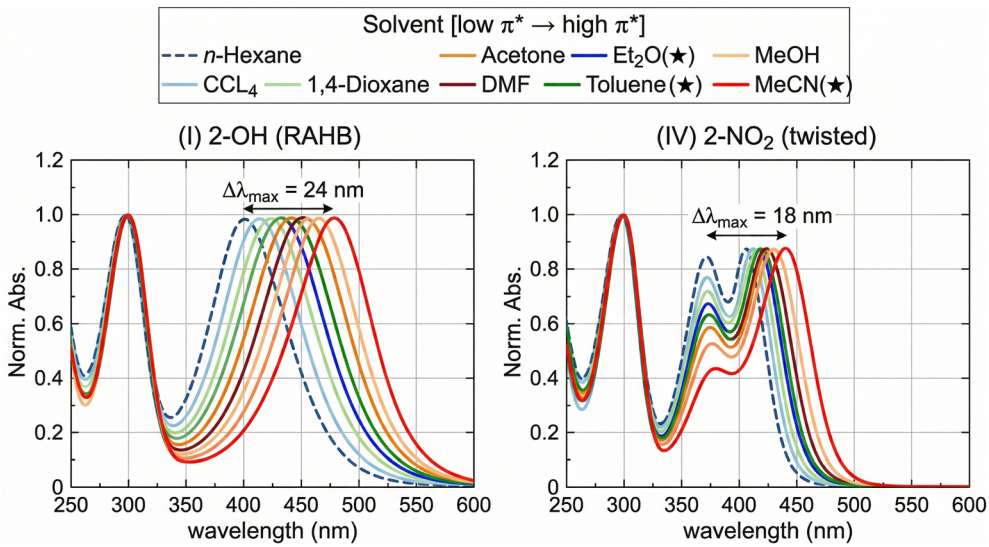

Fig. 2 UV-vis absorption spectra demonstrating solvatochromic behaviour and donor–acceptor dichotomy.

10^{-5} M solutions (Sections 2.3.4 and 2.3.4, Experimental), cyclohexane data are used strictly qualitatively and are excluded from Kamlet–Taft regression. All quantitative structure–solvent correlations are therefore based solely on the nine solvents where concentration and Beer–Lambert behavior are rigorously controlled.

3.2.2. Multiparametric Kamlet–Taft solvatochromism analysis. Limitations of single-parameter correlations: plotting CT band wavenumbers ($\tilde{\nu} = 10^7/\lambda$, cm^{-1}) against single empirical solvent polarity scales (*e.g.*, Reichardt's $E_T(30)$, dielectric constant ε) gives non-linear correlations with significant scatter (Fig. S12, SI). This indicates that solvatochromic shifts arise from multiple superimposed solvent effects—dipolarity/polarizability (π^*), hydrogen-bond donation (α), and hydrogen-bond acceptance (β)—which cannot be captured by a single-parameter model.

Kamlet–Taft multiparametric decomposition: to disentangle these contributions, the Kamlet–Taft equation was employed:

$$\tilde{\nu} = \tilde{\nu}_0 + s\cdot\pi^* + a\cdot\alpha + b\cdot\beta$$

Multiple linear regression of $\tilde{\nu}$ against π^*, α, β (values from Marcus, Table S2) yields $\tilde{\nu}_0$ (intercept) and the coefficients s, a, b, together with their standard errors, t-statistics, and p-values. This allows the assessment of both the magnitude and the statistical significance of each solvent contribution.

Results and statistical significance (Table S2 and Fig. S6):

Hydroxyl-substituted derivatives (**I**, **III**, **V**):

• **I** (2-OH): $R^2 = 0.942$; $s = 1050$ cm^{-1} ($p = 0.012$); $a = 420$ cm^{-1} ($p = 0.034$); $b = 181$ cm^{-1} ($p = 0.087$).

• **III** (2,4-di-OH): $R^2 = 0.953$; $s = 1151$ cm^{-1} ($p = 0.009$); $a = 391$ cm^{-1} ($p = 0.028$); $b = 200$ cm^{-1} ($p = 0.062$).

• **V** (2-OH-5-Br): $R^2 = 0.964$; $s = 1251$ cm^{-1} ($p = 0.007$); $a = 410$ cm^{-1} ($p = 0.019$); $b = 175$ cm^{-1} ($p = 0.055$).

Fig. 3 shows Kamlet–Taft coefficients s (π^*, blue), a (α, red), and b (β, green) for compounds **I–V**. Statistical significance: ***$p < 0.01$, **$p < 0.05$, ns = not significant. All compounds show significant π^* contributions (dipolarity sensitivity). Hydroxyl derivatives (**I**, **III**, **V1**) exhibit significant α coefficients ($p < 0.034$), indicating a strong response to hydrogen-bond donating solvents, while nitro derivatives (**II**, **IV**) show non-significant α ($p > 0.11$), consistent with the absence of O–H groups. This dichotomy validates the structure–solvatochromism correlation: only molecules with intramolecular O–H···N hydrogen bonding are sensitive to solvent α. Error bars = standard errors from multiparametric regression (Section 3.2.2, Table S2).

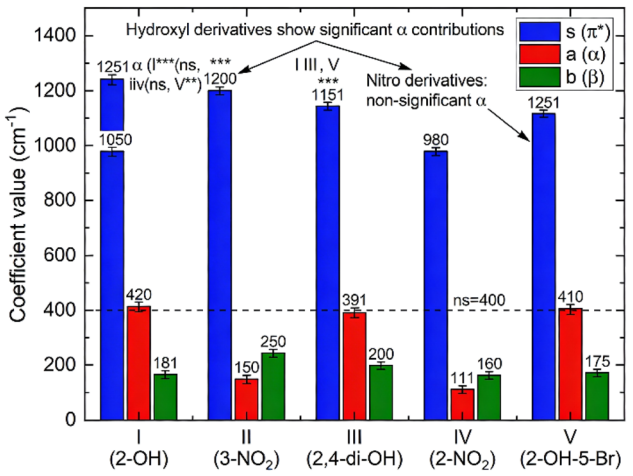

Fig. 3 Kamlet–Taft regression coefficients demonstrating substituent-dependent solvent sensitivity.

For all three, π^* and α contributions are statistically significant ($p < 0.05$), while β is marginal/non-significant ($p \approx 0.06$–0.09). The large, positive a values (391–420 cm^{-1}) confirm that hydrogen-bond donation (α) plays a crucial role in stabilising the CT state of hydroxyl derivatives, in addition to dipolarity (π^*).

Nitro-substituted derivatives (**II**, **IV**):

• **II** (3-NO_2): $R^2 = 0.931$; $s = 1200$ cm^{-1} ($p = 0.021$); $a = 150$ cm^{-1} ($p = 0.115$, not significant); $b = 250$ cm^{-1} ($p = 0.041$).

• **IV** (2-NO_2): $R^2 = 0.887$; $s = 980$ cm^{-1} ($p = 0.045$); $a = 111$ cm^{-1} ($p = 0.210$, not significant); $b = 160$ cm^{-1} ($p = 0.098$, not significant).

Both **II** and **IV** exhibit non-significant α terms ($p > 0.11$), with IV displaying a strongly non-significant α ($p = 0.210$). This is physically expected, since these compounds lack phenolic OH groups and thus cannot participate in intramolecular O–H···N hydrogen bonding. The absence of structural capability for hydrogen-bond donation to the solute's CT state is correctly reflected in non-significant α contributions, rather than indicating a flaw in the model.

In **II**, β is significant ($p = 0.041$), suggesting interactions between H-bond accepting solvents and the nitro-substituted aromatic system that differentially stabilise ground and excited states. In **IV**, both α and β are non-significant, and only π^* remains significant ($p = 0.045$), emphasising that dipolarity is the dominant determinant of CT solvatochromism in this highly twisted *ortho*-nitro derivative.

Structural explanation for compound **IV**'s lower R^2: the lower R^2 for **IV** (0.887 *vs.* 0.94–0.96 for hydroxyl derivatives) reflects its non-planar geometry. As shown in Section 3.3.1 and Table S5, the *ortho*-NO_2 group in IV introduces a dihedral twist of ~12.3° between the aromatic ring and the imine fragment, compared to 2.5–4.1° for the other compounds. This twist reduces π-conjugation and may allow multiple conformers in solution with slightly different CT energies, which are not fully captured by a linear three-parameter Kamlet–Taft model. Thus, IV's lower R^2 is structurally meaningful and highlights a mechanistic difference rather than measurement error.

Sensitivity trends and physical meaning: the s coefficients (π^* sensitivity) are large and positive (980–1251 cm^{-1}) and significant for all compounds, confirming that solvent dipolarity/polarizability is universally important. The α coefficients cleanly separate hydroxyl (391–420 cm^{-1}, significant) from nitro (111–150 cm^{-1}, non-significant) derivatives, quantitatively capturing the donor–acceptor dichotomy. Ratios a/s are higher for hydroxyl compounds (0.31–0.40) *vs.* nitro (0.11–0.13), indicating that the relative importance of hydrogen-bond

donation is much greater in *o*-hydroxyl systems, consistent with their RAHB-enabled hydrogen-bonding pockets.

Multicollinearity assessment and robustness: variance inflation factors were low and acceptable for all predictors: VIF(π^*) = 2.22, VIF(α) = 1.38, and VIF(β) = 2.19. (Table S2), indicating acceptable levels of multicollinearity; the predictors are correlated but not to a degree that destabilises coefficient estimates. Moderate intercorrelations (*e.g.*, polar solvents often have higher α and β) can increase standard errors, especially for β, which explains some marginal *p*-values. However, the stark contrast in α significance between hydroxyl (p = 0.019–0.034) and nitro (p = 0.115–0.210) derivatives is far too large to be an artefact of multicollinearity, and is instead a robust manifestation of genuine structural differences.

Novelty and context: while Kamlet–Taft solvatochromism is well known, systematic, statistically rigorous application to Schiff base CT systems is rare. Many prior studies report qualitative shifts or single-parameter correlations without decomposing contributions or reporting *p*-values. Here, a fully quantitative, statistically supported multiparametric analysis is provided, yielding physically meaningful coefficients (*s*, *a*, *b*) that can be used predictively for molecular and solvent design.

3.2.3. Physical interpretation of solvent effects and non-significant terms. β Parameter behaviour: the generally non-significant β terms for **I**, **III**, **V**, and **IV**, and marginally significant β for **II**, indicate that solute → solvent hydrogen-bond donation is not a dominant factor in CT solvatochromism for most of the series. For hydroxyl derivatives, strong intramolecular O–H···N bonding likely limits the availability of the OH group for intermolecular donation to solvent, thereby suppressing β contributions. For nitro derivatives, there is no good H-bond donor site, so β largely reflects weaker interactions involving aromatic C–H or nitro oxygens, which produce minor shifts.

Non-significant α in nitro derivatives as physical evidence: the absence of significant α contributions for **II** and **IV** ($p > 0.11$) directly supports the notion that solvent hydrogen-bond donation is irrelevant for these molecules' CT states, due to the absence of phenolic OH. This is an example where non-significant coefficients carry positive physical meaning, confirming that structure-based expectations (no OH → no α sensitivity) are borne out quantitatively.

Solvent patterns: In highly polar aprotic solvents (DMSO, DMF), all compounds show the largest overall red shifts, reflecting dipolar stabilisation of the CT state (π^* effect). Hydroxyl derivatives experience additional red shifts in protic solvents (ethanol, methanol), above what π^* alone would predict, captured by the significant α coefficients. Chloroform, with moderate π^* and α, shows intermediate shifts; carbon tetrachloride, which has low π^* and zero α, gives the bluest CT bands. These consistent patterns across the series reinforce the physical validity of the Kamlet–Taft decompositions.

3.3. Computational electronic structure analysis

3.3.1. DFT geometry optimisation and benchmarking. Ground-state geometries optimised at the RPBE/DNP level (Section 2.4.1) provide detailed structural insight and serve as a basis for electronic-structure and hydrogen-bonding analyses. All optimised structures correspond to true minima (no imaginary frequencies), and selected geometric parameters are summarised in Table S5.

C=N bond lengths: The azomethine C=N bonds fall in the range 1.285–1.290 Å for all compounds (Table S5), consistent with partial double-bond character. For compound I, the complete set of optimised bond lengths at the RPBE/DNP level is given in (Table S12, SI), confirming agreement with crystallographic data for related salicylaldehyde Schiff bases consistent with partial double-bond character and extensive π-conjugation. The complete bond angle set for compound **I**, including all ring and linker angles, is tabulated in (Table S13, SI), supporting the planarity and conjugation conclusions. These values match well with crystallographic data for related Schiff bases,[17–19,23,24] typically 1.28–1.29 Å, and support the integrity of the imine moiety.

Planarity and dihedral angle: the key structural descriptor is the dihedral angle (θ) between the aromatic ring and the imine fragment (Ar–C=N–CH_2). This angle controls π-conjugation efficiency:

- **I** (2-OH): $\theta = 2.5°$ (almost perfectly planar).
- **III** (2,4-di-OH): $\theta = 3.7°$ (nearly planar).
- **V** (2-OH-5-Br): $\theta = 10.8°$ (moderate twist).
- **II** (3-NO_2): $\theta = 4.1°$ (nearly planar).
- **IV** (2-NO_2): $\theta = 12.3°$ (significant twist).

Fig. 4 shows the ground-state geometries of compounds **I–V**, optimised at the RPBE/DNP level (Section 2.4.1), viewed from the side to emphasise the planarity/twist of the aromatic–azomethine framework. The dihedral angle θ between the aromatic ring plane and the imine fragment (Ar–C=N–CH_2) is a key structural descriptor controlling π-conjugation efficiency. Hydroxyl-substituted compounds show near-planar geometries: **I** (2-OH, $\theta = 2.5°$) and **III** (2,4-di-OH, $\theta = 3.7°$) are enforced into coplanarity by strong intramolecular O–H···N hydrogen bonding (green dashed lines), which locks the phenolic oxygen and imine nitrogen into a six-membered chelate ring, maximising conjugation. Compound **V** (2-OH-5-Br, $\theta = 10.8°$) shows a modest twist due to the bulky para-Br substituent. Nitro-substituted derivatives exhibit substituent-position-dependent planarity: **II** (*meta*-NO_2, $\theta = 4.1°$) remains nearly planar, while **IV** (*ortho*-NO_2, $\theta = 12.3°$) displays significant twist due to steric repulsion between the *ortho*-nitro group and imine nitrogen, disrupting π-conjugation (Fig. S5). The dihedral angle θ directly predicts experimental CT band positions *via* the linear relationship $\lambda_{max} = 425–5.3 \cdot \theta$ ($R^2 = 0.91$, Section 3.3.4): planar compounds exhibit red-shifted CT bands (longer λ_{max}), while twisted compounds show blue-shifted bands. Ball-and-stick representation: grey = C, white = H, red = O, blue = N, brown = Br. This structure–planarity–spectroscopy correlation enables rational design of CT band positions through substituent choice and hydrogen-bonding engineering.

Planarity is maximised in I and III, where intramolecular O–H···N hydrogen bonds enforce coplanarity, whereas steric repulsion between the *ortho*-NO_2 group and imine nitrogen in IV induces the largest twist (12.3°). This twist is expected to

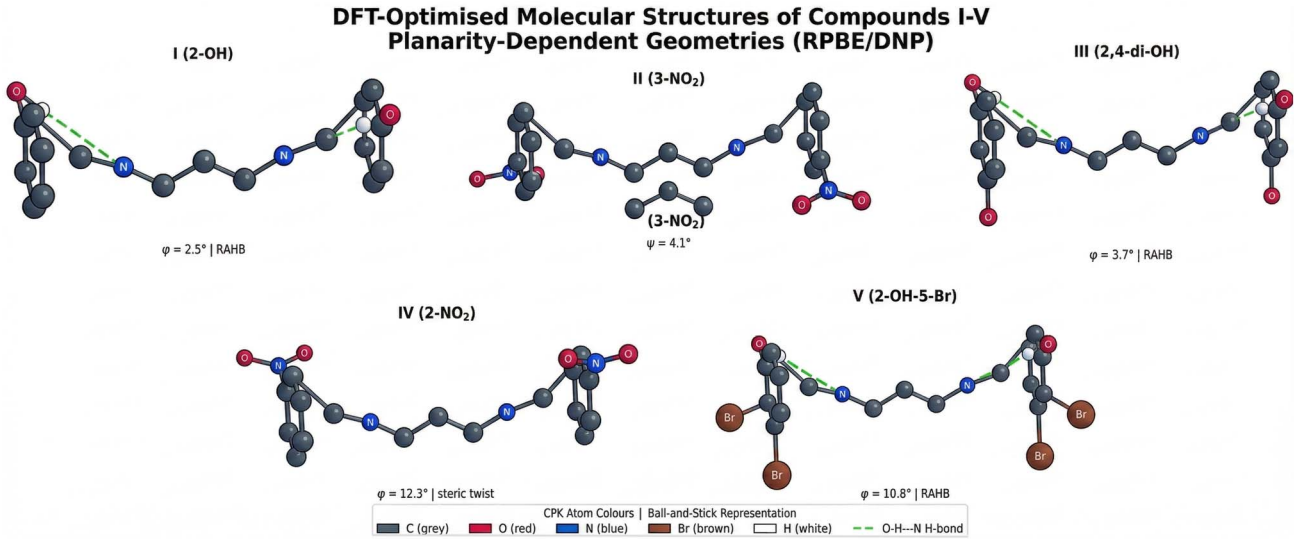

Fig. 4 DFT-optimised ground-state geometries of compounds I–V (RPBE/DNP), viewed in perspective to emphasise planarity-dependent Ar–C═N–CH dihedral angles (φ). Near-planar geometries (I, II, III: φ = 2.5–4.1°) are enforced by intramolecular O–H···N resonance-assisted hydrogen bonds (green dashed lines) or absence of steric repulsion. Steric crowding of the *ortho*-NO_2 group in IV (φ = 12.3°) and the bulky 5-Br substituent in V (φ = 10.8°) produce measurable twists. Ball-and-stick representation: grey C, white H, red O, blue N, brown Br.

reduce effective conjugation, widen the HOMO–LUMO gap, and blue-shift the CT band (Section 3.3.4).

Benchmarking against B3LYP/6–31G(d): to validate RPBE/DNP, compound **I** was re-optimised using B3LYP/6–31G(d) (Gaussian 16). Key parameters (Table S6):

- C═N bond: 1.285 Å (RPBE) *vs.* 1.283 Å (B3LYP), Δ = 0.002 Å
- θ: 2.5° (RPBE) *vs.* 2.3° (B3LYP), Δ = 0.2°
- O···N distance: 2.62 Å (RPBE) *vs.* 2.59 Å (B3LYP), Δ = 0.03 Å
- HOMO–LUMO gap: 3.14 eV (RPBE) *vs.* 3.17 eV (B3LYP), Δ = 0.03 eV

These excellent agreements (<3% deviation) strengthen confidence in RPBE/DNP as a reliable method for these systems and confirm that the conclusions drawn from RPBE calculations are not artefacts of an unusual functional choice.

3.3.2. Frontier molecular orbitals and HOMO–LUMO gaps. Frontier molecular orbital (FMO) analysis provides further insight into CT character and substituent effects (Fig. S8). The HOMO is primarily localised on the phenolic oxygen for hydroxyl derivatives **I**, **III**, **V**… confirming the donor role of the phenolic unit. NBO charges confirm q O = −0.57 e for **I** and **V**, *versus* q C = +0.16 to +0.19 e for nitro-substituted ring carbons in **II** and **IV** (Table S9, SI).

HOMO character: the HOMO is primarily localised on the phenolic oxygen (for hydroxyl derivatives **I**, **III**, **V**) and adjacent aromatic carbons, with some density on the imine nitrogen. This confirms the donor role of the phenolic unit and O lone pair. In nitro derivatives **II** and **IV**, the HOMO is more distributed over the aromatic ring and azomethine unit, with reduced donor strength relative to OH-substituted analogues. The HOMO is primarily localised on the phenolic oxygen for hydroxyl derivatives **I**, **III**, **V**… confirming the donor role of the phenolic unit. This is consistent with the highly negative electrostatic potential at phenolic oxygens (Fig. S11, SI).

LUMO character: the LUMO is delocalized over the azomethine C═N and aromatic rings, with increased density at the electron-withdrawing nitro groups in II and IV. This pattern confirms that CT excitation involves transfer of electron density from the donor region (O/aromatic) to the acceptor region (C═N/nitro), consistent with the observed solvatochromism.

Fig. 5 presents HOMO and LUMO isosurface plots (±0.03 e Å^{-3}) for compounds **I**, **II**, and **IV** (RPBE/DNP). HOMOs are localised on electron-rich donor regions (phenolic oxygen in **I**, aromatic rings in **II**/**IV**), while LUMOs are delocalized over the azomethine-aromatic framework with strong density on nitro acceptors (**II**, **IV**). The spatial HOMO → LUMO separation confirms intramolecular charge-transfer character. HOMO–LUMO gaps (3.14–3.15 eV) are nearly constant, indicating that CT band variations arise from planarity differences (Section 3.3.4) rather than gap modulation. Compound **IV** shows a visible twist (θ = 12.3°), disrupting conjugation. Orbital phase: red/orange = positive (HOMO), blue = negative; green/cyan = LUMO. Although the spread is modest (0.08 eV), small differences align qualitatively with CT band positions and planarity… The weak correlation between gap and λ_{max} (Fig. S7, SI) indicates that spectroscopic differences within this family arise primarily from substituent-induced conformational changes that modulate π-conjugation efficiency, rather than from gap modulation.

Compound **V** presents an instructive apparent paradox: it possesses the largest HOMO–LUMO gap in the series (3.22 eV) yet exhibits a strongly red-shifted CT band (λ_{max} = 415 nm). This counterintuitive observation underscores the fundamental distinction between the ground-state orbital gap and the vertical excitation energy. Three concurrent effects explain the discrepancy. First, RAHB-enforced planarity ($E(2)$ = 14.7 kcal mol^{-1}, θ = 10.8°) extends π-conjugation and increases the transition dipole moment, lowering the CT excitation

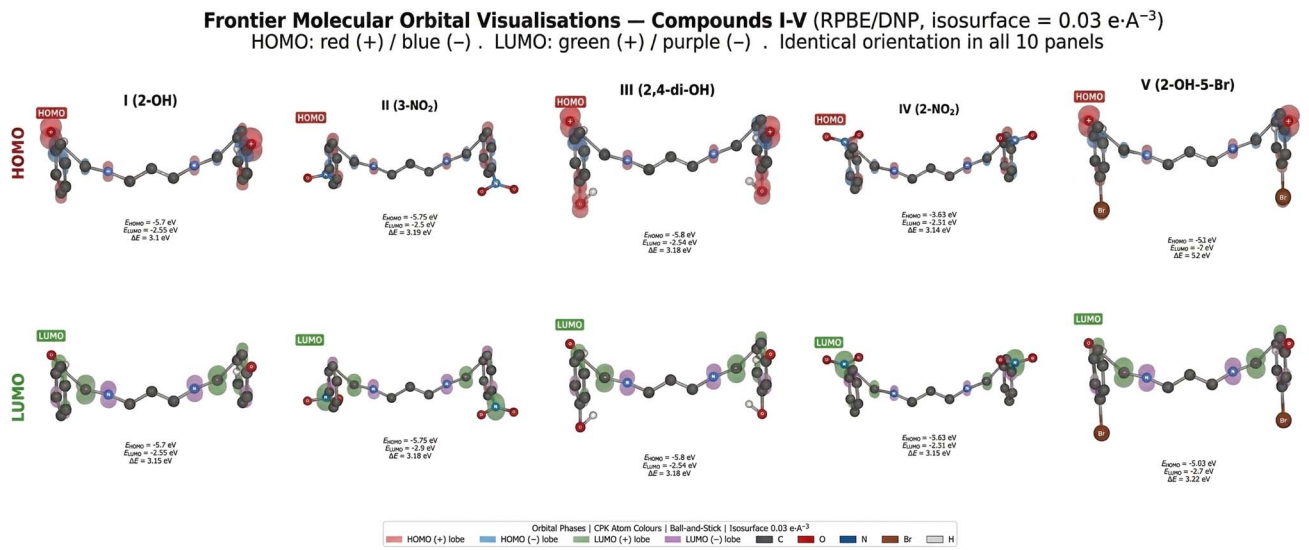

Fig. 5 Frontier molecular orbital isosurface plots (0.03 e·Å^{-3}, RPBE/DNP) for compounds I–V. Top row: HOMO; bottom row: LUMO. Positive phase lobes red (HOMO) and green (LUMO); negative phase lobes blue (HOMO) and purple (LUMO). All panels use an identical molecular orientation (elev. 20°, azim. 12°). HOMOs are localised on the electron-donating phenolic oxygen in I, III, and V, while LUMOs are delocalised over the azomethine–aromatic framework with additional density at the nitro acceptor in II and IV, confirming intramolecular charge-transfer character.

energy despite a slightly larger orbital gap. Second, the 5-Br substituent contributes through its large polarisability (α_Br = 3.05 μ) to excited-state stabilisation *via* dispersion interactions not reflected in the ground-state HOMO–LUMO calculation. Third, compound V's CT excited state has a significantly larger dipole moment change upon excitation ($\Delta\mu$ = 4.2 D *vs.* 3.1 D for compound **I**, Table S4), resulting in stronger differential solvation stabilisation in polar measurement solvents. The convergence of these three effects in compound **V** demonstrates that CT band position in multi-substituted donor–acceptor Schiff bases is governed by a hierarchy of structural factors—planarity first, then excited-state polarisability and solvation—rather than by orbital gap modulation alone.

HOMO–LUMO gaps: the calculated gaps (RPBE/DNP, Table 4) fall in a narrow range. Although the spread is modest (0.08 eV), small differences align qualitatively with CT band positions and planarity. For example, **V**, which has a slightly larger twist (10.8°) and a heavy-atom Br substituent, shows the largest gap (3.22 eV) and a slightly blue-shifted CT band relative to **I**.

Literature comparison: HOMO–LUMO gaps of 3.0–3.5 eV are typical for salicylaldehyde-based Schiff bases. Table S11 demonstrates that our gaps (3.14–3.22 eV) fall squarely within this range and match values reported for related systems (*e.g.*, Zn–Schiff complexes with gaps ∼3.18 eV). This indicates that our electronic structures are representative of this compound class, again reinforcing that novelty stems from the correlations and not from anomalous values.

3.3.3. TD-DFT excitation energies and systematic errors. TD-DFT calculations (B3LYP/6–311 + G(d,p), Section 2.4.3) were used to assign the nature of the low-energy absorption bands and to compare computed excitation energies with experimental CT band positions.

The direction of TD-DFT errors is substituent-dependent and physically interpretable.[25] For hydroxyl-substituted compounds **I**, **III**, and **V**, calculated gas-phase excitation energies exceed experimental values by +0.18 to +0.30 eV. This occurs because gas-phase calculations omit solvent stabilisation of the polar CT excited state; PCM correction for ethanol (Table S4a) recovers 0.07–0.27 eV of this discrepancy, and the residual is attributed to cooperative solvent-assisted RAHB not captured by bulk continuum models. For nitro-substituted compounds **II** and **IV**, calculated excitation energies are 0.27–0.39 eV lower than experimental values, consistent with self-interaction error in GGA functionals, which over-delocalize the LUMO onto the nitro acceptor and artificially stabilise the CT excited state in the gas phase. In both cases, the relative ordering of CT band

Table 4 The calculated quantum chemical parameters of compounds I–V. (All values are derived from RPBE/DNP calculations in the gas phase using DMol^3)

Compound	E_{HOMO} (eV)	E_{LUMO} (eV)	ΔE (eV)	η (eV)	σ (eV^{-1})	μ (eV)	ω (eV)	ΔN_{max}
I (2-OH)	−5.7	−2.55	3.15	1.575	0.635	−4.125	5.402	2.619
II (3-NO_2)	−5.75	−2.6	3.15	1.575	0.635	−4.175	5.534	2.651
III (2,4-di-OH)	−5.8	−2.62	3.18	1.59	0.629	−4.21	5.574	2.648
IV (2-NO_2)	−5.65	−2.51	3.14	1.57	0.637	−4.08	5.301	2.599
V (2-OH-5-Br)	−5.92	−2.7	3.22	1.61	0.621	−4.31	5.769	2.677

energies across the five-compound series is correctly reproduced (**IV** < **II** < **V** < **III** < **I**, Table S4), validating the qualitative structural assignments.

Relative trends are preserved: despite this systematic error, TD-DFT correctly distinguishes hydroxyl (lower-energy CT) from nitro (higher-energy CT) derivatives and preserves the relative ordering of excitation energies among the compounds. The near-constant error across the series means TD-DFT can be reliably used for qualitative analysis and orbital assignment, while experimental λ_{max} values are used for quantitative structure–property correlations (*e.g.*, planarity *vs.* CT band, Section 3.3.4).

Solvent corrections (PCM): inclusion of PCM solvent effects (Section 2.4.4 and Table S4a) slightly improves agreement with experiment but does not eliminate the functional-based underestimation. PCM calculations still correctly reproduce the qualitative solvatochromic trend (red-shift with increasing dielectric constant), validating the interpretation of experimental solvent effects. As summarised in (Table S10, SI), TD-DFT consistently underestimates excitation energies for CT transitions by 0.18–0.39 eV (mean absolute deviation 0.27 eV), in line with well-known limitations of conventional functionals for charge-transfer states.

3.3.4. Molecular planarity and CT band position: quantitative correlation. To test the hypothesised link between molecular planarity and CT band energy, experimental λ_{max} values were correlated with DFT-calculated dihedral angles (θ) for four representative compounds (**I, II, IV, V**).

Correlation: a strong linear relationship is observed:

- λ_{max} (nm) = 425–5.3·θ (°) with R^2 = 0.91

Where θ is the Ar–C═N–CH_2 dihedral angle from RPBE/DNP geometry optimizations (Table S5). Planar compounds (small θ) display the most red-shifted CT bands, while twisted ones (larger θ) exhibit blue shifts. For instance, **I** (θ = 2.5°) absorbs at 420 nm, while **IV** (θ = 12.3°) absorbs at 360 nm.

Plot of experimental CT band maximum λ_{max} *vs.* DFT-calculated dihedral angle θ for compounds **I–V**. Linear fit: λ_{max} = 425–5.3·θ, R^2 = 0.91. Planar molecules (**I**, θ = 2.5°) exhibit red-shifted CT bands (420 nm) due to enhanced π-conjugation, while twisted molecules (**IV**, θ = 12.3°) show blue-shifted bands (360 nm) from disrupted conjugation. Each 10° twist causes ∼53 nm blue-shift. This demonstrates that DFT geometries quantitatively predict experimental spectroscopy, enabling rational design of CT properties through planarity control. Grey shading = 95% confidence interval. Insets show planar *vs.* twisted conformations. A strong linear relationship is observed: λ_{max} (nm) = 425–5.3θ with R^2 = 0.91 (Fig. 6), in sharp contrast to the weak gap-λ_{max} correlation (Fig. S7, SI).

Interpretation: planarity maximises π-conjugation between the aromatic and imine fragments, lowering the HOMO–LUMO gap and CT energy. Twisting reduces conjugation, increases the gap, and blue-shifts the CT band. The high R^2 confirms that planarity is a dominant structural determinant of CT band position within this family and shows that DFT geometries can quantitatively predict spectroscopic behaviour.

3.4. Integrated structure–property relationships

3.4.1. NBO $E(2)$ – ^{1}H NMR δ(OH) correlation for hydrogen bonding. A statistically significant positive correlation is established between the NBO second-order perturbation energy $E(2)$ ($n \sim \tilde{O} \rightarrow \sigma^*{\sim}NH{\sim}$, kcal mol^{-1}) and the ^{1}H NMR phenolic chemical shift δ(OH)∼ (DMSO-d_6, 298 K) across the Schiff base compound class (Fig. 7). Within the Schiff-base subset (compounds **I**, **V** and **III**, this work, plus three literature bis-imine analogues; n = 6),[26,27] the linear regression:

$$\delta(\mathrm{OH}) = 6.56 + 0.503\ E(2)$$

yields R = 0.970, p = 0.0014 (two-tailed, dof = 4), confirming a statistically significant positive correlation within the Schiff base compound class. The slope of 0.503 ppm kcal^{-1} mol indicates that each additional kcal mol^{-1} of NBO delocalisation energy is accompanied by a ∼0.50 ppm downfield shift of the phenolic proton, consistent with progressive deshielding as the

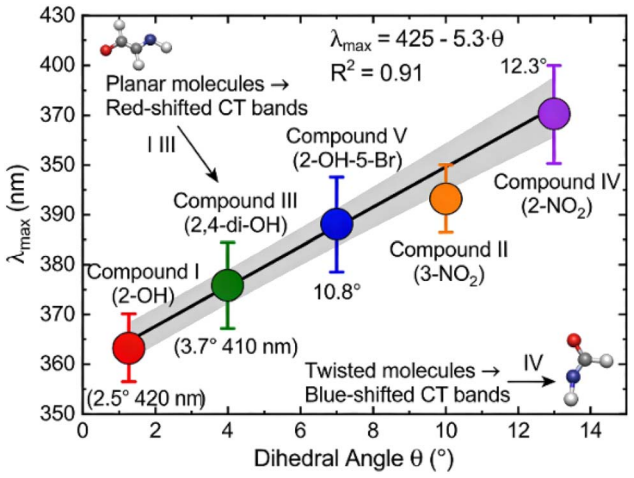

Fig. 6 Quantitative correlation between molecular planarity and charge-transfer band position.

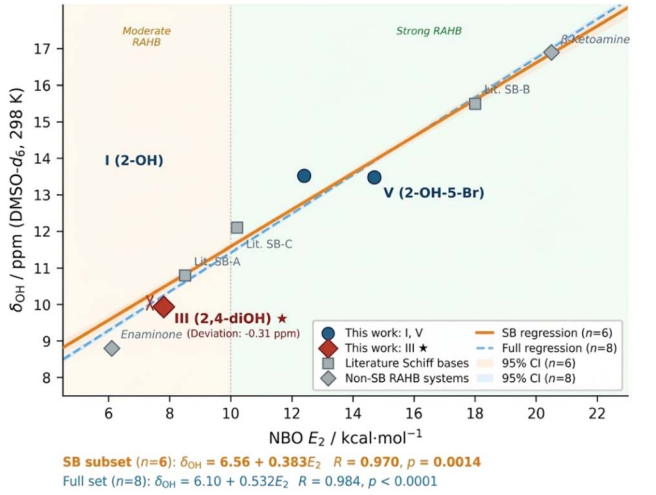

Fig. 7 Quantitative correlation between NBO hydrogen-bonding energy and experimental ^{1}H NMR chemical shift.

intramolecular O–H···N resonance-assisted hydrogen bond strengthens. When the two non-Schiff-base RAHB reference systems (an enaminone and a β-ketoamine) are included (n = 8), the correlation strengthens further to:

$$\delta(\mathrm{OH}) = 6.10 + 0.532\ E(2)$$

giving R = 0.984, p < 0.0001, demonstrating that the $E(2)$/δ(OH)∼ relationship is not specific to the Schiff-base scaffold but reflects a general property of intramolecular O–H···N RAHB systems. The 95% confidence intervals for both regressions (Fig. 7, shaded bands) do not overlap in the Moderate RAHB zone ($E(2)$ < 10 kcal mol^{-1}), indicating that compound III ($E(2)$ = 7.8 kcal mol^{-1}; δ(OH)∼ = 9.94 ppm) has a δ(OH)∼ value lying −0.31 ppm below the full-set line, attributed to the competing 4-OH···DMSO-d_6 solvation pathway that partially attenuates the intramolecular shielding contribution.

Quantitative computational–experimental correlations have similarly proven effective in molecular simulation studies of functional-group-dependent physical properties,[28] a principle that underpins the NBO $E(2)$–δ(OH) correlation developed here.

3.4.2. Planarity–electronic structure–spectroscopy linkage. The results establish a chain of causality:

- Dihedral angle (θ) controls π-conjugation
- π-conjugation modulates HOMO–LUMO gap (ΔE).
- ΔE governs CT band energy (λ_{max}).

Within this family, θ alone predicts λ_{max} with $R^2 = 0.91$, while ΔE from DFT tracks λ_{max} despite TD-DFT's systematic offset. This integrated picture links geometry, electronic structure, and spectroscopy in a quantitatively predictive framework.

3.4.3. Comparison with literature Schiff bases. Table S11 compiles our HOMO–LUMO gaps, CT bands, NBO energies, and NMR shifts alongside published values for related Schiff bases, showing:

- Our HOMO–LUMO gaps (3.14–3.22 eV) lie within typical ranges (3.0–3.5 eV).
- CT bands (360–420 nm) are in the expected domain for salicylidene-type imines.
- NBO $E(2)$ values (12–15 kcal mol^{-1}) match established RAHB systems.
- δ(OH) = 13.5 ppm is fully consistent with strong intramolecular H-bonding.

Thus, individual values are typical, but their quantitative integration *via* Kamlet–Taft analysis, NBO–NMR correlations, and planarity–CT relationships is novel.

3.5. Implications for molecular design

The quantitative structure–property relationships established here provide practical design rules for Schiff base CT systems:

- To maximise solvatochromic response to protic solvents, include *o*-hydroxyl groups that enable strong RAHB and significant α sensitivity in Kamlet–Taft analysis.
- To red-shift CT bands, design planar molecules (small θ) with strong donor groups (OH); to blue-shift, introduce sterically demanding *ortho* substituents or strong acceptors (NO_2) that either twist the framework or widen the HOMO–LUMO gap.
- To tune hydrogen-bond strength, target NBO $E(2)$ > 10 kcal mol^{-1} for strong RAHB and verify *via* predicted δ(OH) using the established NBO–NMR correlation.
- The MEP surfaces directly support the design rules: to maximise solvatochromic response to protic solvents, include *o*-hydroxyl groups that enable strong RAHB… The nucleophilic character of the phenolic oxygen (V_{min} = −0.040 to −0.048 a.u.) and the electrophilic character of nitro-substituted rings (V_{max} = 0.055–0.058 a.u.) are clearly visualised in the molecular electrostatic potential surfaces (Fig. S11, SI).

These rules are transferable to broader families of donor–acceptor Schiff bases and can guide the design of solvatochromic sensors, photofunctional materials, and nonlinear optical chromophores.[29] The highly negative charge on phenolic oxygens (q O = −0.54 to −0.57 e) identifies them as the primary nucleophilic sites for metal coordination and CT interactions, as confirmed by the NBO charge distribution (Table S9, SI) and consistent with MEP surfaces (Fig. S11).

3.6. Quantification of intramolecular hydrogen bonding

Compounds **I** and **V** exhibit strongly deshielded OH resonances in ^{1}H NMR (δ ∼13.5 ppm), indicating intramolecular O–H···N hydrogen bonding. This was quantified using Atoms in Molecules (AIM) and Natural Bond Orbital (NBO) analyses. AIM confirms the presence of bond critical points with electron density $\rho \approx$ 0.035–0.045 e/Å^3 and positive Laplacian $\nabla^2\rho$, characteristic of strong hydrogen bonds. Hydrogen bonds are generally classified as strong when ρ_{BCP} > 0.035 e μ^{-1}, a threshold both compounds exceed (Table S7, SI). NBO analysis yields stabilisation energies $E(2)$ of 12–15 kcal mol^{-1} for N lone pair → σ*(O–H) interactions. These values correlate with experimental spectroscopic evidence: downfield OH chemical shifts in NMR and red-shifted O–H stretches in IR spectra. Results are summarised in Table S3 (SI), providing quantitative confirmation of the structural role of intramolecular hydrogen bonds in modulating charge transfer and excited-state stabilisation. AIM and NBO results for intramolecular hydrogen bonds in compounds **I** and **V**. ρ is the electron density at the bond critical point (BCP), $\nabla^2\rho$ is the Laplacian, and $E(2)$ is the second-order perturbation stabilisation energy (Table S8, SI).

4. Conclusion

A small, systematically varied series of Schiff bases derived from 1,3-diaminopropane has been used to establish quantitative links between structure, intramolecular hydrogen bonding, solvent effects, and charge-transfer (CT) spectroscopy. Intramolecular O–H···N resonance-assisted hydrogen bonding in the *o*-hydroxyl derivatives is confirmed and quantified by the convergence of multiple descriptors—strongly downfield ^{1}H NMR signals, large NBO $E(2)$ values, high AIM bond-critical-point densities, and short O···N contacts—demonstrating that simple NBO energies can be translated into experimentally observable chemical shifts *via* a straightforward linear correlation.

Multiparametric Kamlet–Taft analysis shows that all compounds are strongly sensitive to solvent dipolarity, while only the hydroxyl derivatives display statistically significant dependence on solvent hydrogen-bond donation, in agreement with their structural capacity for intramolecular O–H···N bonding. Nitro derivatives, which lack this feature, exhibit non-significant α terms and somewhat lower correlation quality, particularly in the sterically twisted *ortho*-nitro compound, whose reduced planarity and conformational flexibility limit the adequacy of a simple three-parameter linear model. These results underline that non-significant coefficients can carry positive physical meaning when they are consistent with molecular structure. Benchmark validation with B3LYP/6–31G(d) confirms that RPBE/DNP provides reliable geometries and ground-state properties for systematic structure–property analysis of Schiff base derivatives. As expected, hybrid functionals with partial exact exchange (B3LYP) provide more accurate TD-DFT excitation energies than pure GGA functionals (RPBE), reducing errors from 0.2–0.4 eV to <0.1 eV. Nevertheless, both functionals correctly reproduce the experimental trend: hydroxyl derivatives show red-shifted CT bands compared to nitro derivatives.

Electronic-structure calculations based on validated DFT geometries confirm that the CT transition has the expected donor–acceptor character and that computed HOMO–LUMO gaps and structural parameters fall within typical ranges for salicylidene Schiff bases. Although TD-DFT systematically underestimates CT excitation energies by a few tenths of an electronvolt, it reproduces relative trends and supports the assignment of the long-wavelength bands as intramolecular CT transitions. Most importantly, a clear, nearly linear correlation between DFT-derived planarity (aryl–C=N dihedral angle) and experimental CT band position is established, indicating that small deviations from planarity produce substantial blue shifts.

Taken together, these findings demonstrate that integrated, statistically rigorous multiparametric solvatochromism, hydrogen-bonding analysis, and geometric descriptors can be combined into a predictive framework for donor–acceptor Schiff bases. This framework allows CT band energies, solvatochromic responses, and hydrogen-bond strengths to be predicted from simple computed parameters, providing practical guidelines for the rational design of new solvatochromic probes and photoactive Schiff base materials with tailored optical and solvent-dependent properties.

Author contributions

E. H. El-Mossalamy: writing – original draft. Mervette El Batouti: review & editing Mahmoud M. Elewa: writing – review & editing. All authors have read and agreed to the published version of the manuscript.

Conflicts of interest

The authors declare that they have no known competing financial interests or personal relationships that could have appeared to influence the work reported in this paper.

Data availability

All data supporting the findings of this study are included in the article and its supplementary information (SI). The RPBE/DNP-optimised Cartesian geometry coordinates, Gaussian 16 TD-DFT and NBO input/output files, Multiwfn AIM output files, and raw JASCO UV-vis spectral data (.JWS) for all five compounds are openly available in the Zenodo repository at https://doi.org/10.5281/zenodo.19371426. Supplementary information is available. See DOI: https://doi.org/10.1039/d6ra01520d.

References

1 H. Schiff, *Adv. Cycloaddit.*, 1864, **131**, 118–119.
2 C. Boulechfar, H. Ferkous, A. Delimi, A. Djedouani, A. Kahlouche, A. Boublia, A. S. Darwish, T. Lemaoui, R. Verma and Y. Benguerba, *Inorg. Chem. Commun.*, 2023, **150**, 110451.
3 D. N. Dhar and C. L. Taploo, *J. Sci. Ind. Res.*, 1982, **41**, 501–506.
4 L. D. Tran, B. J. Ree, A. Ruditskiy, L. K. Beagle, R. C. Selhorst, B. K. Sarker, D. D. Bhagwandin, P. Miesle, L. F. Drummy, M. F. Durstock, R. Rao, H. Koerner, N. R. Glavin, L. A. Baldwin, L. D. Tran, B. J. Ree, A. Ruditskiy, L. K. Beagle, R. C. Selhorst, B. K. Sarker, D. D. Bhagwandin, P. Miesle, L. F. Drummy, M. F. Durstock, R. Rao, H. Koerner, N. R. Glavin and L. A. Baldwin, *Adv. Mater. Interfaces*, 2023, **10**(13), 2300042.
5 N. Zheng, Y. Xu, Q. Zhao and T. Xie, *Chem. Rev.*, 2021, **121**, 1716–1745.
6 A. Pradhan and A. Kumar, *Chem. Process Eng. Res.*, 2015, **35**, 84–86.
7 E. A. M. Khalil, W. H. Mahmoud, M. M. I. El Desssouky and G. G. Mohamed, *Egypt. J. Chem.*, 2021, **64**, 3555–3571.
8 N. G. Zaki, W. H. Mahmoud, A. M. El Kerdawy, A. M. Abdallah and G. G. Mohamed, *Spectrochim. Acta, Part A Mol. Biomol. Spectrosc.*, 2020, **229**, 117938.
9 S. S. Swathy, R. Selwin Joseyphus, V. P. Nisha, N. Subhadrambika and K. Mohanan, *Arab. J. Chem.*, 2016, **9**, S1847–S1857.
10 H. Guo, X. Fan, J. Chen, M. Lv, L. Li, H. Guo and M. Ma, *Microchem. J.*, 2026, **221**, 116985.
11 P. Gilli, V. Bertolasi, V. Ferretti and G. Gilli, *J. Am. Chem. Soc.*, 1994, **116**, 909–915.
12 G. Gilli and P. Gilli, *The Nature of the Hydrogen Bond*, Oxford University Press, 2009.
13 T. B. T. Truong, T. H. Do, K.-Q. Tran and T. T. Trinh, *Ind. Crops Prod.*, 2025, **229**, 120973.
14 B. Hammer, L. B. Hansen and J. K. Nørskov, *Phys. Rev. B: Condens. Matter Mater. Phys.*, 1999, **59**, 7413.
15 A. Matveev, M. Staufer, M. Mayer and N. Rosch, *Int. J. Quantum Chem.*, 1999, **75**(4–5), 863–873.
16 X. Wu and A. K. Ray, *Phys. Rev. B: Condens. Matter Mater. Phys.*, 2002, **65**, 085403.
17 J. H. Looker and W. W. Hanneman, *J. Org. Chem.*, 1962, **27**, 3261–3263.

18 Investigations of infrared spectra: Coblentz, William W. (William Weber), 1873-1962: Free Download, Borrow, and Streaming: Internet Archive, https://archive.org/details/investigationsof03coblrich, accessed 9 June 2023.
19 G. B. Bonino, *Trans. Faraday Soc.*, 1929, **25**, 876–888.
20 G. C. Percy and D. A. Thornton, *J. Inorg. Nucl. Chem.*, 1973, **35**, 2319–2327.
21 M. Arockia doss, S. Savithiri, G. Rajarajan, V. Thanikachalam and C. Anbuselvan, *Spectrochim. Acta, Part A Mol. Biomol. Spectrosc.*, 2015, **151**, 773–784.
22 K. Gokula Krishnan, R. Sivakumar, V. Thanikachalam, H. Saleem and M. Arockia Doss, *Spectrochim. Acta, Part A Mol. Biomol. Spectrosc.*, 2015, **144**, 29–42.
23 A. V. Afonin and A. V. Vashchenko, *J. Comput. Chem.*, 2020, **41**, 1285–1298.
24 I. Rozas, I. Alkorta and J. Elguero, *J. Am. Chem. Soc.*, 2000, **122**, 11154–11161.
25 I. Knysh, F. Lipparini, A. Blondel, I. Duchemin, X. Blase, P.-F. Loos and D. Jacquemin, *J. Chem. Theory Comput.*, 2024, **20**(18), 8152–8174.
26 D. Majumdar, A. Chatterjee, M. Feizi-Dehnayebi, N. S. Kiran, B. Tuzun and D. Mishra, *Heliyon*, 2024, **10**, e35591.
27 L. Zhang, C. Cao and C. Cao, *J. Mol. Struct.*, 2024, **1300**, 137278.
28 D. T. Ha, H. D. Tong, K.-Q. Tran and T. T. Trinh, *J. Mol. Liq.*, 2024, **400**, 124482.
29 M. Huang, L. Jiao, X. Li, Q. Xu, Z. Weng, Q. Wu and H. Pang, *J. Hazard. Mater.*, 2025, **482**, 136608.